# Remote Awareness of Image Quality for Multiweek Shore-Launched AUV Surveys

**ADRIAN BODENMANN**[1], **DANIEL O. B. JONES**[2], **ALEXANDER B. PHILLIPS**[3],
**ROBERT TEMPLETON**[3], **RASHIID SHERIF**[3], **FRANCESCO FANELLI**[3],
**DARRYL NEWBOROUGH**[4], **AND BLAIR THORNTON**[1,5] **(Member, IEEE)**

[1]Centre for In Situ and Remote Intelligent Sensing, University of Southampton, SO17 1BJ Southampton, U.K.
[2]Ocean BioGeosciences, National Oceanography Centre, SO14 3ZH Southampton, U.K.
[3]Marine Autonomous and Robotic Systems, National Oceanography Centre, SO14 3ZH Southampton, U.K.
[4]Sonardyne International Ltd., GU46 6GD Yateley, U.K.
[5]Institute of Industrial Science, The University of Tokyo, Tokyo 153-8505, Japan
CORRESPONDING AUTHOR: ADRIAN BODENMANN (adrian.bodenmann@soton.ac.uk)

*(Regular Article)*

**ABSTRACT** Visual seafloor imaging using autonomous underwater vehicles (AUVs) has become an established method for seafloor mapping and monitoring. With AUVs now achieving multiweek endurance and several hundred kilometers of range on a single charge, image quality assessment (IQA) on-board vehicles in the field is necessary for robust data acquisition given the sensitivity of underwater imaging surveys to environmental conditions. This research develops a metric to assess seafloor image quality in situ, and demonstrates its use for quality assurance during a 21-day, shore-launched AUV campaign that visited three sites up to 170 km from shore. The metric was transmitted via satellite communication along with vehicle telemetry to shore-based AUV operators during regular surfacing intervals without relying on physical vehicle recovery. The method was implemented on the seafloor laser scan and strobed imaging system BioCam, deployed on the Autosub Long Range (ALR) AUV (also known as Boaty McBoatface) in the North Sea. Several tens of hectares of seafloor imagery were collected, and image quality scores were transmitted. This information was used to retask the AUV and maximize the quality of acquired images within operational constraints. Data products generated from the collected imagery show the improvements achieved that would otherwise have been missed. This highlights the importance of remote awareness of data quality to facilitate longer and consecutive mapping missions without reliance on physical vehicle recovery.

**INDEX TERMS** Autonomous underwater vehicles (AUVs), environmental monitoring, image quality, low-bandwidth communication, photogrammetry.

## I. INTRODUCTION

THE past ∼40 years have seen the development of various autonomous underwater vehicle (AUV) mapping techniques [1], [2] to enable large-scale, high-resolution monitoring of seafloor environments. In particular, camera-equipped AUVs operating several meters off the seafloor can gather millimeter-resolution images in which human-made objects and benthic organisms can be identified, over multihectare regions of the seafloor. These are valuable for surveying marine protected areas (MPAs) that require regular monitoring of their ecosystem health, and for inspecting the increasing amount of seafloor infrastructure that exists, with growing recognition of the need to monitor their environmental impacts. The push toward offshore renewables, demand for subsea cables to support the Internet, and legal requirements for decadal monitoring of decommissioned offshore oil and gas infrastructure suggest the need for seafloor imaging surveys will continue for the foreseeable future [3]. While

traditional methods using sampling and drop cameras provide information that cannot be replicated using AUVs, they do not scale well to large-area surveys as they rely on ships and manual labor. Seafloor imaging lends itself better to automation, where images gathered by AUVs can be post-processed to generate products such as mosaics [4], [5], and 3-D reconstructions [6], [7], [8] that show areas larger than a single image footprint. Further analysis by human experts or machine learning algorithms [9], [10] can determine seafloor substrate type, taxonomy, and distributions of seafloor organisms, as well as detect anthropogenic influences such as litter, sabotage, or degradation of infrastructures. High-resolution imaging surveys can also capture temporal changes through precisely targeted repeat area surveys that are noninvasive and achieve sufficient cover to guarantee spatial overlap despite navigational uncertainties [11]. Laser scan microbathymetry is an effective complement to strobed color photography as it can simultaneously map topography at millimeter-order resolution alongside visual features to capture fine details such as cables, natural depressions, and trawl marks that often are hard to spot in strobed color images [12].

Offshore AUV surveys typically deploy from crewed ships that use several orders of magnitude more energy than an AUV, accounting for most of the cost, logistical challenges, and carbon footprint of monitoring. AUVs have also been deployed from autonomous surface vehicles (ASVs) [13], [14], with recent investments in full ocean-going lean crewed ships with AUV payloads [15]. However, autonomous launch and recovery adds complexity and limits operations to relatively calm weather windows. Recently, long-range and endurance AUVs have demonstrated shore-launched offshore surveys without the use of a support vessel for transport [16], [17], [18], [19]. Such AUVs open the opportunity for ship-free seafloor visual mapping of sites hundreds of kilometers offshore. In addition to cost and carbon savings, shore-deployed long-range AUVs are more robust to poor weather conditions. Close to shore the wave height and wind speed are generally lower than on the open sea, and once deployed, AUVs can shelter at depth if necessary to avoid strong winds and waves that can prevent traditional ship-based deployment and recovery operations. However, such missions introduce several new challenges for data acquisition, analysis, and robust operation without physical intervention.

The impact of water turbidity on image quality makes camera surveys more sensitive to environmental conditions than acoustic survey methods (e.g., side-scan sonar and multibeam sonar). Typically, turbidity is not known before deployment and can vary locally and temporally, making the choice of observation altitude in long-range, long-endurance surveys a challenge. This is compounded by long-range flight-style AUVs being less maneuverable, and traveling faster than the hover-capable AUVs typically used for detailed imaging surveys [20], [21], [22], [23], [24], [25], [26]. They therefore need to operate at higher altitudes to reduce the risk of collisions and cannot accurately follow complex terrains at a constant target altitude. Both factors increase the variability of image quality and sensitivity of data they acquire to environmental variables (i.e., terrain complexity and water turbidity).

Various approaches have been developed to correct for attenuation, color shift, and backscatter in underwater images [6], [10], [27], [28], [29]. Although these improve tolerance to image degradation, they cannot compensate for information that is lost through attenuation or masked by backscatter of the light from vehicle-mounted strobes if the water turbidity and/or the mapping altitude is too high, or if the camera signal is weak or not resolved sufficiently high. With these requirements in mind, the University of Southampton and Sonardyne International developed the BioCam [30] mapping device with high-power strobes (2 × 200 000 lumen) and line lasers (2 × 1 W), and cameras with a high dynamic range (79.7 dB). This allows data to be collected from higher altitudes than conventional imaging systems and improves robustness to the impact of the large range of altitudes expected when mapping from high-endurance flight-style AUVs such as the Autosub Long Range (ALR; also known as Boaty McBoatface) developed by the National Oceanography Centre (NOC), Southampton, U.K. [18], [19].

In addition to hardware design, it is also necessary to modify operational workflows. During traditional ship-based AUV imaging, operators often assess the quality of images between deployment cycles and can adjust camera parameters (camera exposure and strobe intensity) and target altitude if navigational data indicates it is safe to do so. This also identifies hardware failures (e.g., of the illumination sources) to avoid taking unnecessary risk and effort by continuing to deploy a compromised setup.

To achieve similar goals with long-range AUV campaigns, it is necessary to assess the gathered data between dives and regularly feed it back to remotely located AUV pilots, who can, in turn, adjust mapping altitude or device settings, or navigate it back to shore early if there is any failure of hardware (e.g., illumination light sources). This also requires indicators about navigational performance to determine whether changes in observation altitude would be safe. While for ship-based missions or deployments close to shore full image and navigation data can be downloaded and assessed between dives, this is not possible in offshore missions without a support vessel. Data can be transmitted via satellite when the AUV is at the surface; however, with uplink speeds of pressure-tolerant communication antennae typically in the order of kilobits per second and often intermittent connections, it is not practical to transmit entire uncompressed images and vehicle data.

Various approaches have been proposed for compressing underwater images for transmission over low-bandwidth communication links, such as acoustic modems. Early on, Hoag et al. [31] and Eastwood et al. [32] proposed using the discrete wavelet transform (DWT) for compressing subsea photographs and videos for transmission over an acoustic

uplink. Kaeli et al. [33] demonstrated an algorithm for selecting representative images while collecting seafloor photographs to be sent to a surface vessel, along with semantic maps. Murphy et al. [34] presented broadcasting of automatically selected, progressively compressed photographic and SONAR images, as well as sensor data over networks of underwater acoustic relays. Ahn et al. [35] demonstrated image selection and dropout-resistant image compression using a reduced-size color palette for transmission over acoustic links. These methods enable adaptive, remote-supervised missions for mapping particular types of substrates or objects of interest on the seafloor, as seafloor images are available to operators in near real-time. While these show what has been observed, the quality of the gathered imagery can be difficult to assess, due to the effects of compression, and the number of transmitted images can be low in case of slow or intermittent communication. For applications where the area to be mapped is defined from the outset, or if the communication throughput is very low or unstable, transmitting the quality of the gathered imagery together with compressed navigational data is more suitable.

Traditionally, the mean opinion score (MOS) based on the judgment of several human observers has been regarded as the best method for assessing the quality of images [36]. However, apart from being time-consuming and not suited to autonomous applications, the MOS is subjective and therefore not generally repeatable. To overcome these limitations, various image quality assessment (IQA) algorithms have been developed. Some of these, so-called full-reference IQA algorithms, compare images to a perfect, not distorted version of the image as reference, while blind or no-reference IQA algorithms compute a score without such reference, only based on a single image.

The blind image quality index (BIQI) [37] is a two-stage no-reference IQA algorithm that identifies the types of distortions in an image and combines their respective impacts on quality based on natural scene statistics (NSSs). Distortion identification-based image verity and integrity evaluation (DIIVINE) [38] extends BIQI with a larger set of NSS, demonstrating comparable correlation with human perception to full-reference IQA algorithms. The learning-based blind image quality measure (LBIQ) [39] uses machine learning to map natural image measures and texture statistics to subjective image quality scores, achieving a good correlation with human judgment-based scores. The popular blind/referenceless image spatial quality evaluator (BRISQUE) algorithm [40] computes statistics of pixel intensity distributions and determines how natural an image is by comparing its coefficients to those of a model generated from training images. The natural image quality evaluator (NIQE) [41] like BRISQUE also uses a space domain NSS model, but does not rely on human-judged images for training or modeling of image distortions. Perception-based image quality evaluator (PIQUE) [42] is an opinion-unaware no-reference IQA method that estimates the quality for blocks of pixels while also computing and over-all score by pooling the separate block scores. While these algorithms were developed considering degradation influences characteristic for images taken in air, underwater images also suffer from shifts in color balance, changing lighting across the scene depending on the distance from the camera, haze from backscatter, and marine snow. These influences are often stronger than image compression artifacts, sensor noise, and blur of objects outside the depth of field, typically considered in conventional IQA algorithms. For this reason, IQA algorithms specially for underwater images have been developed.

Many earlier underwater IQA algorithms are based on feature engineering, where a combination of features designed by humans are assessed and combined to generate a score. The underwater color image quality evaluation (UCIQE) algorithm [43] combines statistical measures of chroma, contrast, and saturation to compute a score. The underwater image quality measure (UIQM) [44] and the frequency domain UIQA metric (FDUM) [45] each defines a quality measure using the colorfulness, sharpness, and contrast of underwater images. The colorfulness, contrast, and fogdensity (CCF) [46] algorithm further accounts for backscatter. The no-reference underwater IQA based on multifeature fusion in color space (NMFC) [47] method uses morphological and statistical parameters of distributions of intensity and color, and the contrast, sharpness, and naturalness (CSN) index method [48] uses multiple contrast coefficients, sharpness, and locally mean subtracted contrast normalized coefficients to determine image quality. More recent methods have used feature learning, where features are algorithmically identified from patterns in the data. The cross-spatial feature interactions and the cross-scale information complementarity (SISC) [49] method uses the ResNet CNN to analyze underwater images at different resolutions to compute a quality score. Prior-based underwater enhanced IQA (PBUIQA) [50] uses a convolutional neural network (CNN) to estimate ambient light, water depth, absorption, and scattering coefficients, as well as the object-camera distance map from a raw image to assess the quality of the color image obtained after color correction.

Many underwater IQA algorithms assess the quality of images after color correction, rather than raw images [43], [44], [45], [46], [47], [48], [49], [50]. This leads to a coupling between raw image quality and the performance of the color correction algorithms, which is undesirable for real-time applications where the aim is to maximize the quality of raw data being acquired. Many algorithms are also geared toward the typical scenes a diver would photograph; often naturally lit and taken from oblique perspectives with an animal or object as its subject. However, images acquired using AUVs typically look vertically down on the seafloor and are illuminated using vehicle-mounted strobes. Such images may also lack distinct objects, showing just the substrate of the seafloor. This makes many established IQA methods unsuitable for systematically obtained wide-area photograph

surveys. In addition, marine snow increases the measured contrast and spectrum of intensities in artificially lit images, raising the issued score of many published methods, even though it degrades the quality of seafloor imagery.

To address these challenges, a simple but robust algorithm was developed that works with downward-looking raw strobed and laser scan seafloor imagery. It aims to express image quality information such as images with a few bytes of data. We demonstrate its use when sent via satellite communication along with filtered navigation data to provide sufficient information for making informed decisions for AUV piloting. Baseline data was collected using the ALR AUV equipped with the BioCam seafloor imaging system during the DY152 cruise in the Celtic Sea in July 2022 [12]. The image assessment algorithm was first used to inform decisions on a shore-launched science campaign as part of the AT-SEA project in September and October 2022 in the North Sea, where two decommissioned oil exploration sites and one MPA were mapped. The campaign comprised two deployments of the same setup as during the DY152 cruise, each lasting approximately ten days, covering a total distance of over 1000 km with no support vessel.

In the remainder of this article the image quality metric is described in Section II and data postprocessing algorithms are explained in Section III. The seafloor mapping device and AUV used to demonstrate the effectiveness of the proposed image metric are introduced in Section IV, along with details on the software integration and the data flow. Results from the 21-day shore-launched campaign are provided in Section V, followed by a discussion and conclusion in Section VI.

## II. IN SITU IMAGE QUALITY METRIC

### A. CONSIDERATIONS OF LIGHT PROPAGATION IN WATER

The limiting factor for the quality (and so largest range) of strobe-lit underwater images is typically backscatter, which is optical noise from light scattered toward the camera in the volume of water where the camera's field of view (FOV) and the light cones from the strobes overlap, as shown in Fig. 1. Scattering occurs when light interacts with water molecules or suspended particles, where the latter can have a much larger contribution to the total amount of scattering. This is typically the case in waters near continents where particle density is high due to sediment influx from river run-off, industrial discharge, or ship traffic in shallow waters. Light is scattered in all directions, at varying proportions depending on the particle size and wavelength. For imaging applications the impact is threefold: Light scattered out of the light source-object-camera path (out-scatter) does not reach the camera and so leads to a reduction in the direct signal. Light scattered toward the camera before reaching the seafloor (backscatter) is added to the image of the scene, appearing as haze or fog; or bright spots if reflected off large particles of marine snow. Light scattered at small angles (forward scatter) also contributes to the image of the scene, however, due to the
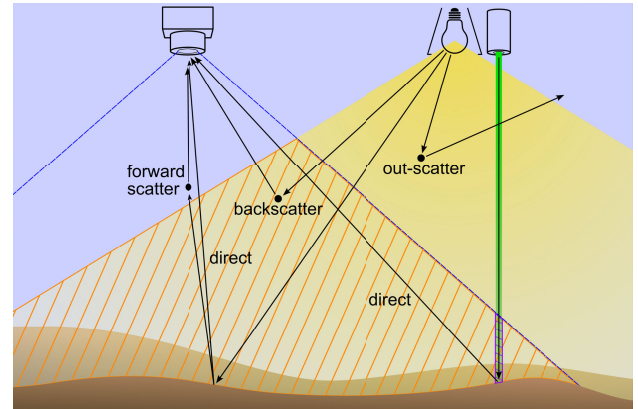


**FIGURE 1.** Illustration of various paths that can be taken by emitted light from an underwater strobe or a sheet laser to the lens of a camera. The rays from the direct light path project the underwater scene on the camera sensor, whereas backscatter adds spurious light, reducing the signal-to-noise ratio of the image. Backscatter occurs where the camera's FOV and the volume illuminated by a light source overlap. The orange hatched area marks the overlap of the camera's FOV with the light cone of a strobe and the purple area shows the overlap with the volume of water illuminated by a sheet laser.

change in direction of the light path it blurs the image. From that follows the image formation model for the irradiance at the camera [51]:

$$E_{\text{total}} = E_{\text{direct}} + E_{\text{forwardscatter}} + E_{\text{backscatter}}. \quad (1)$$

While blurring from forward scattering limits the achievable optical resolution and can impact the performance of high-resolution camera systems, the reduced signal-to-noise ratio from the decreased direct signal compared to haze from backscatter is the more limiting factor for most imaging systems unless the water turbidity is very low. The intensity of the direct signal decreases with increasing distance to the seafloor due to absorption and out-scattering in water, but also due to the spreading of light according to the inverse square law.

Underwater laser scanners, where a laser line is projected onto the seafloor and observed from a camera separated by a certain distance, are also subject to the effects of scattering. However, because of the smaller overlap of the camera's FOV with the laser light sheet as opposed to the light cone in the case of strobed photographs (see Fig. 1), the relative amount of backscatter is significantly smaller. For setups where both types of images are taken sequentially, strobed images are more sensitive to environmental factors, and so constrain the maximum altitude from which sufficient quality data can be acquired.

### B. DEFINITION OF METRICS

To estimate the image quality, we propose a laser projection image-derived quality metric. We assume that the line laser projector(s) is/are aligned with the camera as shown in Fig. 2(a), so that the laser line projections appear as horizontal

lines across the images when scanning a flat area of seafloor. Because turbidity affects the laser line images mainly through out-scatter and less through backscatter, the brightness of the laser line is representative of the water turbidity and reflectivity of the seafloor. It is therefore an indicator for the expected quality of strobed images, as well as the laser line images themselves that can be acquired by a given system and mapping altitude. In contrast to optical backscatter (OBS) point turbidity sensors, the proposed method measures the direct rather than the backscattered component of light reaching the sensor. Although these properties are related, they depend on the particle size, which is normally not known. In addition, OBS sensors do not take the reflectivity of the seafloor into account, which also influences the signal-to-noise ratio in seafloor photographs.

We define the quality score for the laser-projection-based underwater IQA (LUIQA) as the maximum value in a region of interest (ROI) covering the entire height and the central $d$ pixel columns in an image of a raw (unprocessed) laser line projection image $I_{\text{laser}}$

$$q = \max_{\substack{u \in \left[\frac{w-d}{2}, \frac{w+d}{2}\right] \\ \forall v}} (I_{\text{laser}}(u, v)) \tag{2}$$

where $w$ is the width of the image (aligned with the across-track direction of the vehicle), $d$ is the width of the ROI, and $u$ and $v$ designate the pixel coordinates across and down relative to the top left corner of the image, as shown in Fig. 2. While the vertical position of the laser line in the images depends on the vehicle altitude and the bathymetry, using the entire height of the image guarantees that the laser line is captured (as long as it is not occluded, e.g., due to steep terrain features). This provides a direct quality estimate of laser images and indirectly also of strobed images taken at roughly the same time (for the system considered in this research there is a laser line image taken within 0.1 s for every strobed image). However, the quality score does not pick up on potential physical problems with the strobed image collection, such as saturation or failure of the strobes to trigger. To convey this type of information for remote operations, an engineering score $e$ for strobed images is defined as

$$e = \max_{\substack{u \in \left[\frac{w-d}{2}, \frac{w+d}{2}\right] \\ \forall v}} (I_{\text{strobed}}(u, v)) \tag{3}$$

where $I_{\text{strobed}}$ is a raw strobed image, assumed to have the same dimension as images of the laser projection.

While the ROI covers the entire height of the image, the width is limited to the $d$ columns in the center, as the area below the vehicle's axis is illuminated most evenly and so leads to a uniform performance across different altitudes, and reduces the computational load. The impact of the width of the ROI on the quality measure was investigated using a set of randomly sampled images acquired by the AUV-camera system described in Section IV in the Greater Haig Fras MPA
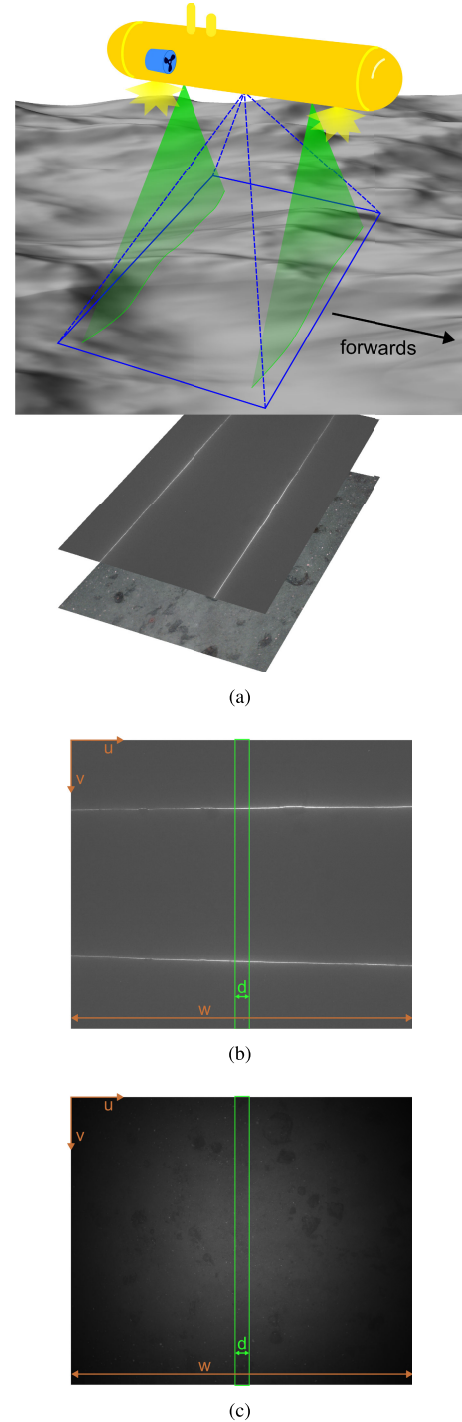


FIGURE 2. Considered mapping system setup with examples of a laser line image and a strobed image. (a) Configuration of image acquisition system with the camera FOV shown in blue, the laser projections in green, and strobes in yellow, as well as an example of a monochrome image of the laser projections and an example of a strobed color photograph (after debayering and color correction). (b) Monochrome image of the laser line projections with an ROI with $d = 100$ indicated in green and the image coordinate system and dimension in brown. (c) Raw strobed image (color image prior to debayering) with an ROI with $d = 100$ indicated in green and the image coordinate system and dimension in brown.

during RRS *Discovery*'s DY152 cruise whilst maintaining a constant altitude from the seabed. With the quality score $q$ defined as the maximum brightness inside the ROI, it is designed to identify the brightness of a pixel showing the laser line projection. If the ROI is narrow, the chances of particles suspended in the water occluding the laser line projection are increased. On the other hand, larger particles in the water can also appear as bright spots in the image if they happen to be in the plane illuminated by the laser, and in the camera's FOV. Widening the ROI increases the chances of picking up such outliers. Fig. 3(a) shows that the quality scores are stable for narrow ROI widths of around 10 pixels (i.e., covering 0.32° across), with outliers appearing increasingly for widths larger than 100 pixels (i.e., covering 3.2° across).
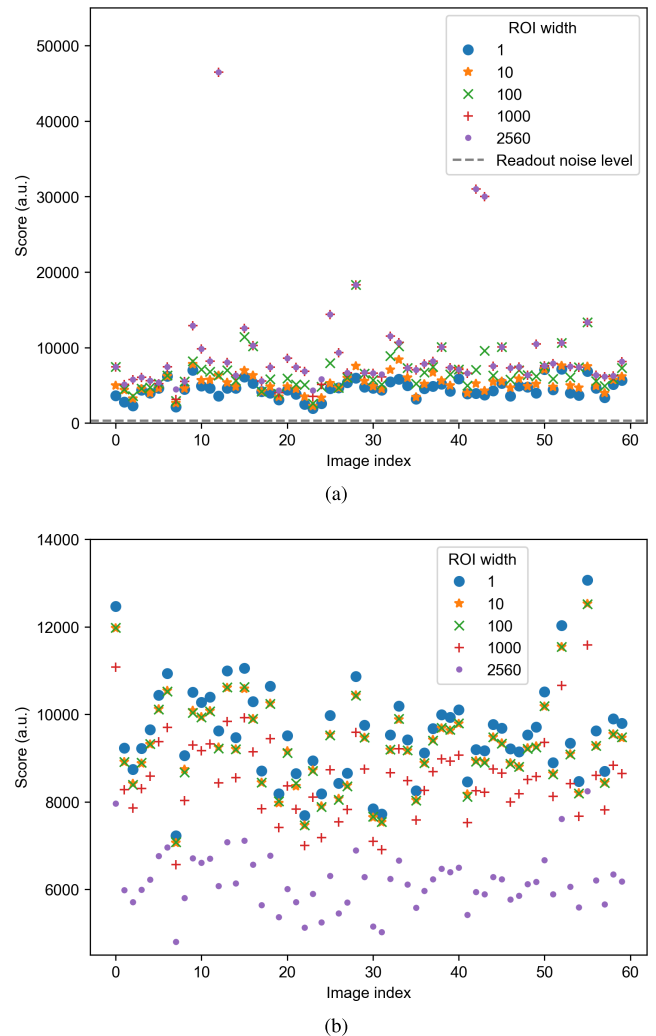
As the engineering score $e$ for strobed images is based on the average brightness within the ROI, it is less sensitive to outliers but as Fig. 3(b) shows, changing the width of the ROI leads to a scaling effect. The reason for the reduction in the mean brightness and so of the engineering score when widening the ROI is that lens vignetting causes the brightness of the images to fall off with increasing distance from the center of the image. However, the shape of the result is the same within a reasonable approximation, and as long as the same ROI width is used for reference and real-time collected data, the conclusions that can be drawn are not affected. For these reasons, the width $d$ of the ROI was set to 10 pixels for both types of score, as it reduces the probability of picking up bright outliers in the laser line images while also being robust against occlusions and keeping the computational load low for real-time computation.

While the strobed images are in general uniformly illuminated, the laser line projections are narrow visual features originating from a point source. This makes them susceptible to occlusions, e.g., due to fish or large particles in the water column blocking part of the light path, or terrain features obstructing the view of the camera onto the laser projection. Such occlusions often only affect part of the laser projection. By applying the maximum operator on the entire ROI, the score picks up on the unobstructed part of the laser line in the event that part of it is blocked, whereas a measure using an averaging operator (e.g., mean-of-maximum-per-column) would lead to conflating brightness values from obstructed and nonobstructed areas. While it can still happen that the laser projection is not visible at all or an object in the water column leads to a bright spot inside the ROI, the unexpectedly low or high scores would stand out clearly as outliers in a time series and so could be ignored by operators.

### C. REFERENCE SCORES

Reference data from two locations in the southwest approaches with different water turbidities was collected with the ALR-BioCam setup during the DY152 research cruise in the Greater Haig Fras MPA with medium[1] level of water

---

[1] For the sake of simplicity we refer to the different turbidities at the surveyed sites discussed in this article as "low," "medium," and "high." These are used as relative classifiers.



(a)



(b)

**FIGURE 3.** Quality and engineering scores for a set of images using different widths *d* of the ROI used to compute the score. (a) Image quality scores based on laser line images. (b) Image engineering scores based on strobed images.

turbidity and South West Deeps (East) MPA with a low level of turbidity. Fig. 4 shows the image scores from both sites plotted against the image acquisition altitude above the seafloor. For both types of scores there is a clear trend for decreasing scores with increasing altitudes, as expected, as light spreads and gets attenuated with increasing light path length and so reduces the signal from the seafloor. However, the level of turbidity strongly influences the rate at which images degrade with increasing altitude, as is apparent in the images from the different sites and which is correctly reflected in the quality scores. Meanwhile, engineering scores indicate that the strobes were working correctly, without overexposing the photographs, as all scores are well above readout noise levels (approximately 300 for the cameras used), yet far from saturation (65 535). Unlike the laser line image-based quality scores, the strobe-based engineering scores are not as distinctly different in water of different clarity, because in turbid waters where the direct signal is lower, increased backscatter adds to the average brightness.
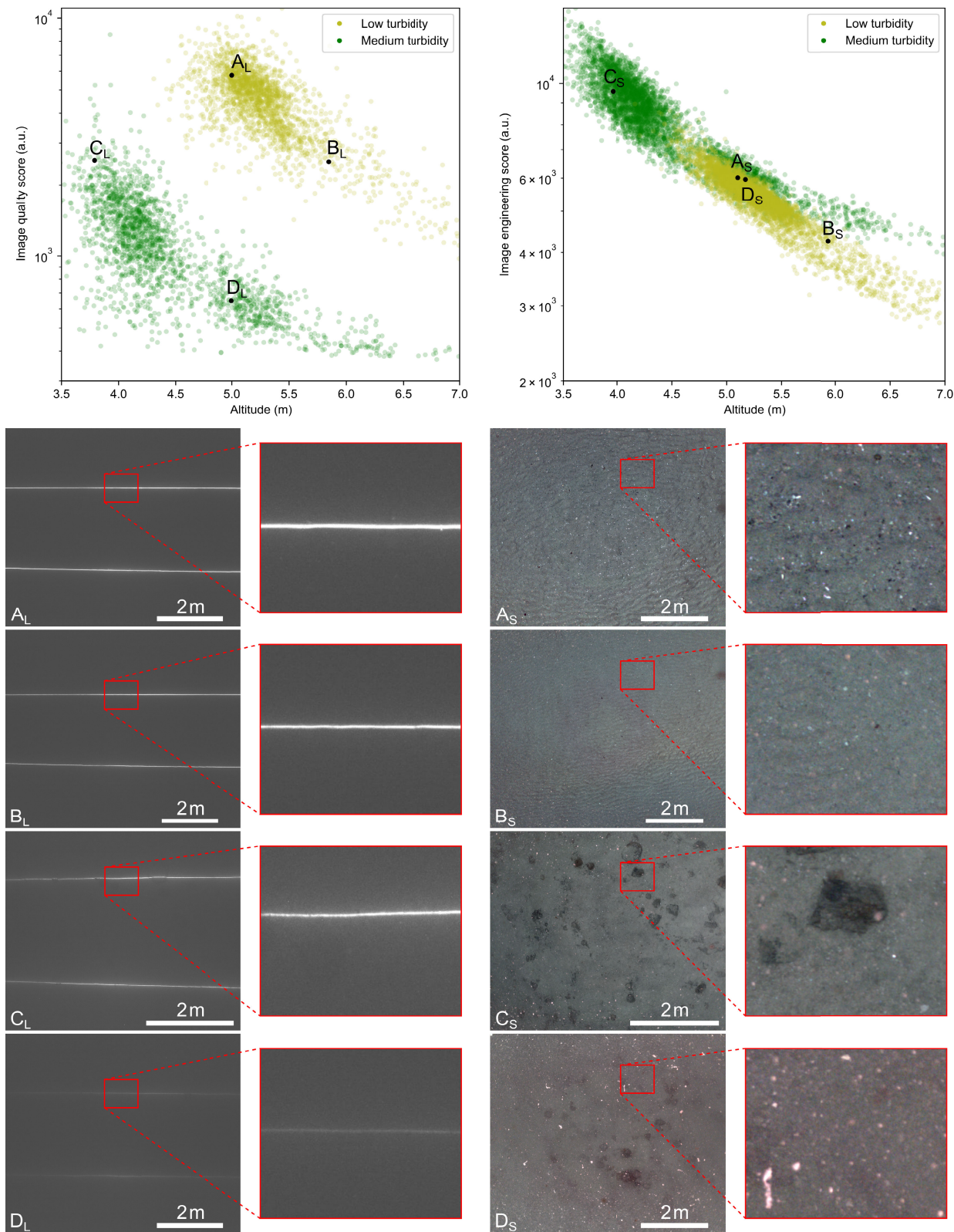
**FIGURE 4.** Quality and engineering scores from two different sites (medium turbidity: Greater Haig Fras MPA and low turbidity: South West Deeps (East) MPA). The images below the plots show examples from four locations, where neighboring laser lines and strobed images are from the same location. The enlargements of the strobed photographs show the varying levels of marine snow appearing as blurred white or reddish spots, with a high density in image $D_S$ and lower densities in $B_S$ and $C_S$. The sharp white spots in $A_S$ are fragments on the seafloor, rather than floating particles.
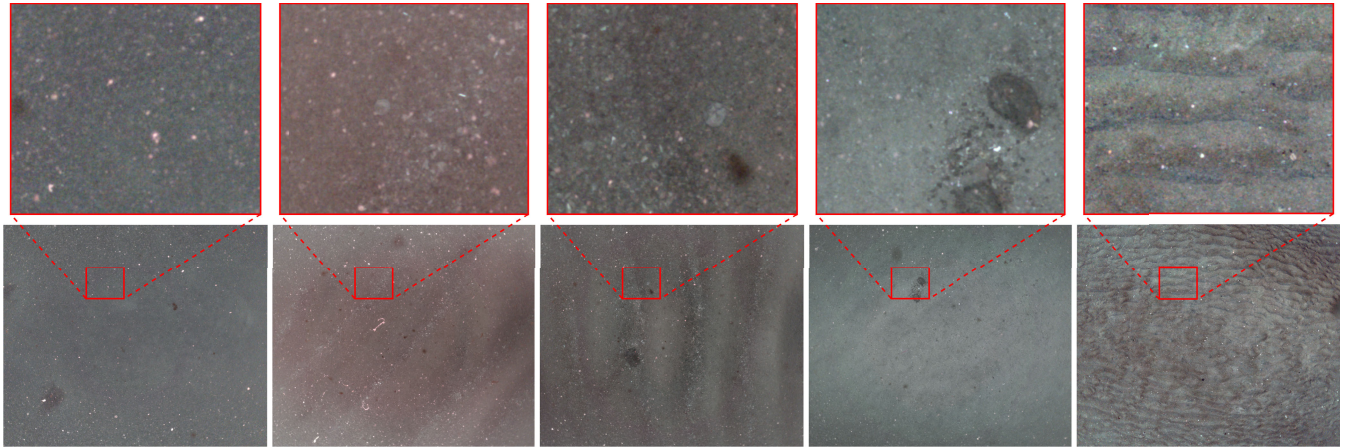
**FIGURE 5.** Examples of strobed color photographs taken under different conditions. The quality scores when these images were taken were 502, 710, 1007, 2025, and 5020 (from left to right). The enlargements show decreasing levels of blurred bright spots from marine snow with increasing quality scores.

The photographs in the bottom half of Fig. 4 show that images taken at the same altitude (A and D) have vastly different image qualities depending on the turbidity of the water with sharp, bright laser line projections (A) and clear views of sand ripples and shells in one location, but at the same altitude in a different location faint blurred laser line projections (D) and strobed images which are bright on average, but dominated by marine snow and turbidity throughout the image. On the other hand, images taken from different altitudes (B and C) but in waters of different clarity can be similar in quality with intermediate brightness of the laser line projections and strobed color images that despite some marine snow appearing as bright dots, offer relatively clear views of the seafloor. Hence the laser-based image quality metric is an effective indicator of image quality for both strobed and laser line illuminated images.

While the method generalizes to any seafloor mapping system collecting laser projections and strobed imagery, the correlation of image score to image quality is characteristic for each setup. Based on the scores for the data collected during the DY152 cruise, these values were determined for the BioCam on ALR setup used to demonstrate the proposed method. Fig. 5 shows strobed images with the corresponding quality scores indicated. The figure shows that for values around 500 the images are very turbid and so are not usable to identify any objects or creatures in them. For values around 700 structures can be recognized, in particular around the center of the image, but marine snow is dominant. For scores around 1000 structures such as sand ripples and objects such as rocks are clearly visible across the entire image. Small objects such as shells can be recognized, but marine snow is also present, in particular around the borders of the image. For scores around 2000 structures and objects are well visible across the entire image, with some marine snow. For scores around 5000 and above images are clear with negligible effects of turbidity. The images in the figure were color corrected with the algorithm described in Section III-B.

## III. DATA POSTPROCESSING

### A. GENERATION OF DIGITAL 3-D RECONSTRUCTIONS OF THE SEAFLOOR

While images are assessed for quality in real-time, they are processed to generate data products in postprocessing. The algorithm described in [8] is used to generate digital 3-D reconstructions of the scanned seafloor based on the laser line and the strobed color photographs. It uses the images of the laser line projection to compute high-resolution bathymetry and the shape of objects on the seafloor, and therefore relies on the line projections being sufficiently clear. After converting the raw strobed photographs to color images with the algorithm described below, they are used to map the color information to the 3-D reconstruction of the seafloor. While the algorithm itself does not depend on the quality of the strobed color photographs, it is important for users of those reconstructions that the strobed photographs are of sufficient quality for organisms, objects, and properties of the seafloor substrates to be discernible in the texture maps that the algorithm generates.

### B. COLOR BALANCING OF STROBED PHOTOGRAPHS

The color images are debayered, attenuation corrected and color balanced based on the method described in [52]. It applies the gray world assumption over the entire image dataset while accounting for the individual distance to the seafloor for every pixel using the 3-D reconstructions to compensate for wavelength-dependent attenuation over the distance the light has traveled in water.

### C. AUTOMATIC CLASSIFICATION OF STROBED IMAGES

In order to automatically classify the mapped areas into areas of the same types of substrate, demersal communities, or areas with similar types of artificial objects, the color photographs are classified using the algorithm described in [9]. It ingests the color-balanced seafloor photographs and is tolerant to limited amounts of image noise, but its ability to

reliably classify images degrades if the quality of photographs that it is presented with decreases. The algorithm identifies clusters in the latent space representation of the images resulting from applying a CNN, and based on this prompts the user to label a number of images that allow it to best delineate the boundaries between classes of similar images. Provided with this information it trains a kernel support vector machine (SVM) with a radial basis function (RBF) to assign labels to all images based on their latent space representation [53].

## IV. SEAFLOOR MAPPING DEVICE AND AUV

### A. BioCam

The seafloor mapping device "BioCam" described in [30] with specifications noted in Table 1 and pictured in Fig. 6 was used to demonstrate the algorithms. It consists of a main housing, two LED strobes, two sheet lasers, and a laser safety float switch. It is designed to be mounted to an AUV supplying power and communication for sending start and stop commands, while strobed images and images of the laser line projection are recorded internally. During data collection, the lasers are triggered simultaneously at 10 Hz and the projected lines are captured by a monochrome camera. The strobes are triggered every 3 s and the images are recorded with both monochrome and color cameras. During exposures when the strobes fire, the lasers are not triggered to avoid the laser projections appearing in the strobed images. The high dynamic range cameras make it possible to correct for strongly varying lighting conditions in postprocessing without having to adapt the exposure or gain during image collection. The duration of both the strobes and lasers can be varied to adapt to different operating conditions. BioCam communicates with the AUV either via serial (RS232) communication or Ethernet to receive commands, send status updates, and synchronize clocks. The status update that is sent once a minute contains the latest image scores, as well as the number of images, current mode, remaining disk space, and CPU and camera temperatures. This information can be used by the AUV, or forwarded to AUV pilots during communication windows, to ensure correct operation of the camera system and monitor data quality.

### B. AUTOSUB LONG RANGE

ALR is a class of ultralong range AUVs developed at the NOC, that can operate for weeks to months in the ocean, depending on their payload. There is a 6000 m depth-rated variant, ALR6000, with up to two months' endurance [18] and a 1500 m depth-rated variant, ALR1500, with an endurance of up to six months [19]. The vehicles are 3.5 m long, 0.8-m diameter, and weigh approximately 1.2 tons. The ALR6000 is built around two 0.71-m outer diameter forged aluminum pressure vessels, the forward of which houses the batteries and the aft contains the primary electronics. Surrounding the pressure vessels is a polypropylene boat frame skinned in a free-flooding glass-reinforced plastic fairing, to provide a hydrodynamic shape. In the free flooding areas



**FIGURE 6. BioCam setup on ALR. The main housing containing the cameras and electronics is mounted centrally. Sheet lasers and LED strobes are mounted one each at the front and the back of the vehicle.**

forward, aft, and between the pressure vessels there is volume available for science payloads.

### C. MECHANICAL INTEGRATION OF BioCam INTO ALR

BioCam was integrated into the 6000 m rated version of ALR. The polypropylene boat frame was redesigned to permit the BioCam camera unit to be installed centrally in the floodable space between the two main pressure spheres, in order to maximize the separation between the main housing and the strobes and lasers. To maintain the stiffness characteristics of the ALR replacement and additional syntactic foam was designed to counteract the low-slung mass of the BioCam. Bespoke hydrodynamic fairings were produced to minimize drag penalties associated with the installation of the BioCam. In addition, an ADCP was mounted in a forward-looking configuration, to provide information on terrain in front of the AUV. Fairings installed between the forward-looking ADCP and the forward strobe assembly, on the ALR abort drop weight, and a Perspex cover over the rear strobe reduce the total drag by almost 10%, compared to not having the fairing, which is important to enable large range deployments to be planned with the desired contingency margin.

With a minimum hotel load, the 6000 m rated ALR has a range of up to 1800 km and an endurance of two to three months. Equipped with BioCam these values are reduced, but by turning BioCam on only when ALR has reached the area of interest, mapping sites several hundred kilometers from the launch and recovery location can be reached.

### D. ALR ONBOARD CONTROL SYSTEM (OCS) AND INTEGRATION WITH BioCam

The ALR OCS has been developed using the robot operating system (ROS) middleware [54]. It adopts a conventional three-layer control architecture, comprising of a supervisory layer consisting of a mission executive, a mission layer responsible for converting mission goals to instantaneous

**TABLE 1. BioCam specifications.**

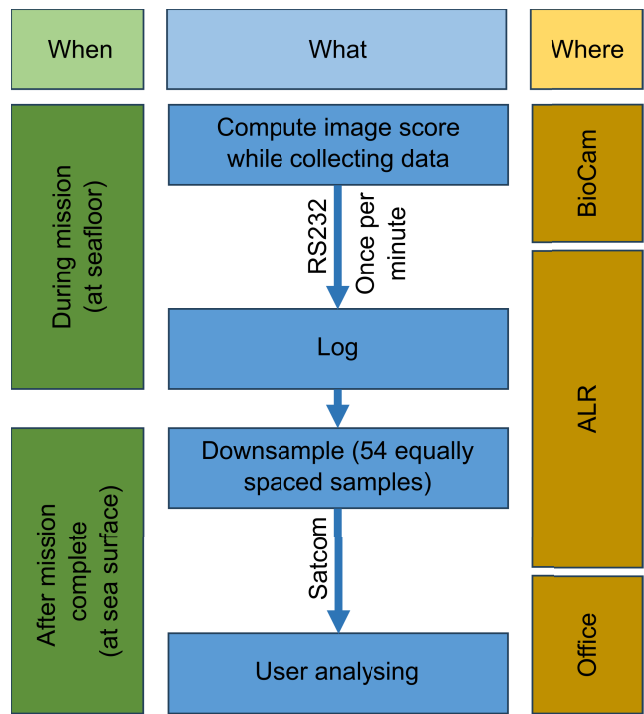| | |
|---|---|
| Weight (in air / in water) | 35.9 kg / 20.2 kg |
| Depth rating | 4000 m |
| Power consumption (typical) | 1.2 A at 48 V |
| Communication | RS232 and Ethernet |
| Cameras | pco.edge 5.5 (1 × monochrome, 1 × colour) |
| Lens | 2 × ZEISS Dimension 2/12, Focal length: 12 mm |
| Camera FOV in water (each) | 69.3° × 60.5° |
| Camera resolution (each) | 2560 × 2160 pixels |
| Image acquisition frequency (typical) | Laser line projection: 10 Hz<br>Strobed: 0.33 Hz |
| Mapping altitude | 4–10 m |
| Storage | 2 TB (60 h of continued data collection) |
| CPU | Intel Pentium N4200, 1.1 / 2.5 GHz |
| Strobe brightness | 2 × 200,000 lumen |
| Sheet laser optical power and wavelength | 2 × 1 W at 525 nm |
| Laser safety | Float switch (→ disabled out of water), Watchdog timer |
| Resolution of 3D reconstructions (for alt. = 5 m, v = 0.75 m/s) | 75 mm along track, 2.8 mm across, 2.5 mm vertical |

control demands, and the vehicle layer which performs real-time control and communicates with hardware devices.

ALR has been developed to support a range of science applications and has been successfully operated both from research vessels and launched from shore. To support this variety of operating modes the vehicle is equipped with three communication channels, WiFi for near operator command and control (C2) on the surface, acoustic communications for near operator C2 subsurface, and Iridium satellite communications for over the horizon C2 when the AUV is on the surface utilizing Iridium short burst data (SBD) messages. Iridium SBD messages are utilized for satellite communication because of their short transmission time, which makes them robust for AUVs operating in rough conditions where antenna wash over is a regular occurrence. However, reliance on SBD messages for over-the-horizon operation does restrict the available bandwidth; the ALRs 9522B modem provides 1860 bytes uplink and 1920 bytes downlink in a single message. For each communication method the human–machine interface is provided by the Oceanids C2 system [55].

Across all communication channels, four distinct message types are currently supported. While designed primarily for the Iridium channel, the size of the message can be tailored to match the available channel constraints as follows.

1) *Instant Commands (Uplink):* Used to manage payload power and settings and trigger specific preprogrammed behaviors (e.g., 'surface,' 'stop' or 'abort').

2) *Mission Scripts (Uplink):* Contain a sequence of maneuvers that the AUV will conduct sequentially. Typically a mission script will comprise of a dive, followed by a sequence of tracks defining a trajectory between two waypoints for the AUV to traverse at a specific depth/altitude followed by a surface maneuver.

3) *Status Messages (Downlink):* Status messages provide an instantaneous snapshot of the AUVs state including parameters such as the pose of the vehicle or the distance to the current target during a mission. A limited amount of space can also be used to send deployment-specific payload data. Status messages are transmitted periodically by the vehicle on all the available channels (WiFi, acoustic, and satellite), with an independently configurable transmission period and content for each channel.

4) *Mission Summary (Downlink):* This message is automatically generated and sent on completion of a mission. As the name suggests, it provides a summary of the behavior of the AUV during a mission, and one of its main aims is to provide the operator with a quick and effective means to assess the performance of the vehicle during a mission when piloting over the horizon (i.e., when access to the complete onboard logs is not available). Mission summaries contain both statistics of engineering and payload data collected throughout the whole mission (such as the maximum depth or the average battery voltage), and an additional series of statistics computed over smaller time intervals obtained by subdividing the total mission into 54 sections of equal length. The number of sections was determined to maximize the data slices that can fit into a single Iridium message, which together offer a sufficiently fine-grained resolution for simple remote analysis of the vehicle behavior. Both the average and minimum altitude in each section are transmitted to facilitate efficient assessment of the safety of low-altitude mapping operations. The altitudes are encoded in a custom format where the resolution is dropped to 10 cm, which
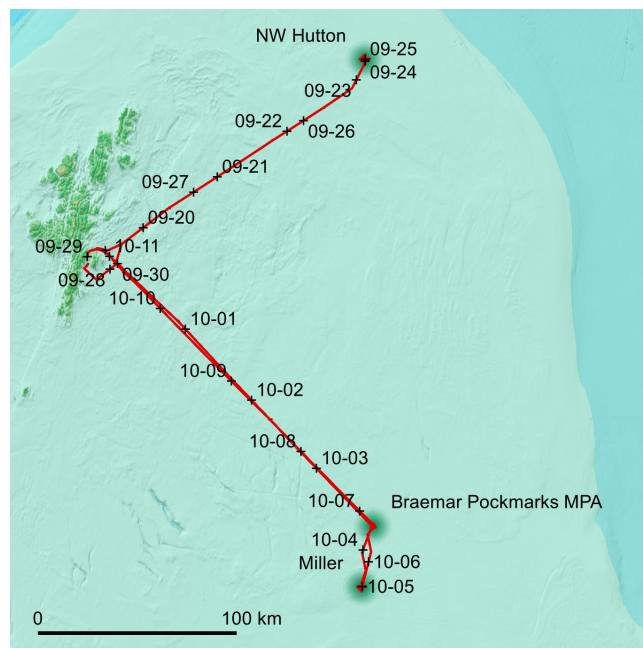
FIGURE 7. Flow of information for image scores transmitted via summary messages.



FIGURE 8. AUV track of the two-legged deployment out of Lerwick, Shetland. The crosses indicate where the AUV was at 0:00 of the indicated date (month-day in 2022).

is sufficient for safety-relevant assessment, but reduces the number of bits occupied in the transmitted bitstream. Fields are reserved to enable the integration of deployment-specific data. On missions where BioCam is used, these fields are populated with the latest BioCam image scores for each of the 54 time windows. These are retrieved from the logged scores that BioCam sends to ALR once per minute throughout the mission, and transmitted with the other vehicle data, as illustrated in Fig. 7.

### E. OVER HORIZON OPERATION OVERVIEW

During operations, the AUV is programmed to carry out a mapping dive, where the mapping altitude is set by identifying the most suitable tradeoff between the swath-width of the camera's FOV and resolution per pixel for the mission, factoring in expected visibility but also vehicle safety to ensure the AUV does not collide with the seafloor or objects on it. If after the dive the spread of the image scores received via satellite communication is at satisfying levels compared to the reference scores in Section II-C and the minimum altitudes are close (within approximately 0.5 m) to the set altitude, the following dives can be carried out with the same settings. However, if the image quality scores are low, the mapping altitude may be lowered for the next dive, if there is sufficient margin in the altitude keeping and other information about the dive site suggests it is safe to do so. On the other hand, if the altitude data shows unexpectedly low values or if image scores suggest lighting hardware failure, the AUV may be sent back to shore early for analysis of the full data.

## V. RESULTS

In September and October 2022, ALR-BioCam was deployed on two shore-launched deployments from Lerwick on Shetland, U.K., to monitor two decommissioned oil extraction sites and one MPA. The aim of the campaign was to demonstrate gathering data for environmental monitoring of offshore sites without a support vessel. The survey areas were up to 170 km from the launch site. The campaign was split into two legs, where the surroundings of the decommissioned rig at the North West Hutton oilfield were visited on the first leg and the decommissioned production site at the Miller oilfield, as well as the Braemar Pockmarks MPA in the second leg, as shown in Fig. 8. Multiple dives were carried out at each decommissioned site, between which ALR transmitted data via Iridium SBD packages while at the surface. Dives were planned based on multibeam echosounder (MBES) bathymetry maps collected during a survey by MRV *Scotia* operated by Marine Scotland Science in June 2021 and charts provided by BP. Since artificial structures still protruded from the seafloor in the areas of interest, missions were initially planned with a mapping altitude of 5 m above the seafloor. This was relatively high considering the expected visibility at the sites, but was set to minimize the risk of the AUV getting stuck with no ship in the vicinity to track the vehicle's position underwater or salvage the AUV.

After being towed out of the harbor by a small boat, ALR transited at 30 m depth at an in-water speed of between 0.5 and 0.6 m/s toward the dive sites, and surfaced once per day to obtain a GPS fix, report telemetry to the pilots and take updates for the next waypoint. On leg 1 of the campaign, it reached the remains of the North West Hutton oil platform after four days. After completion of the first 12-h long
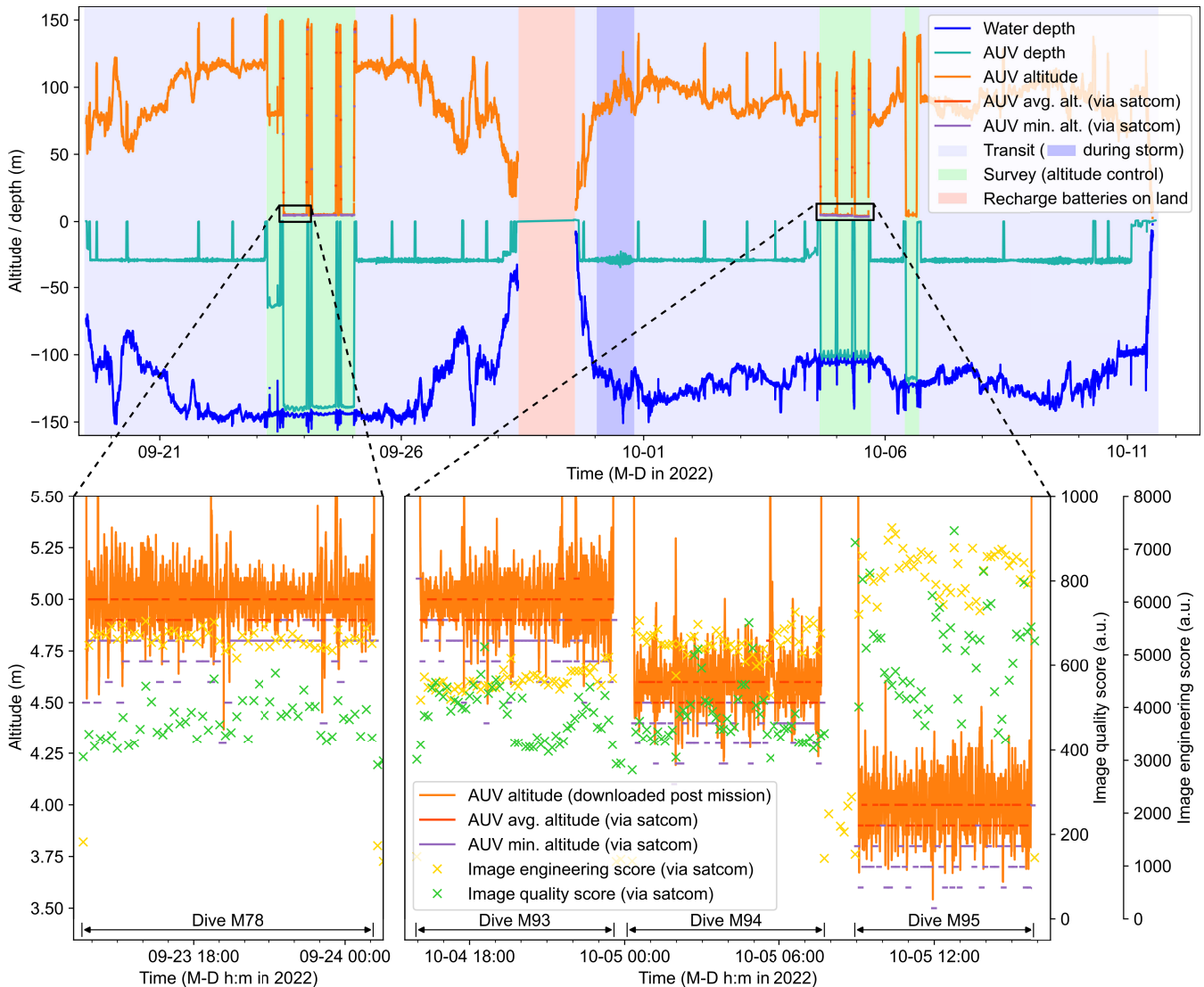
**FIGURE 9.** Plot of navigational data and image scores transmitted by the AUV over satellite communication and full data downloaded postrecovery of the vehicle. The enlargement on the left shows details of the first dive at the NW Hutton site and the enlargement on the right data from the three dives at the Miller site.

mapping dive (M78), the mission summary containing the subsampled BioCam image quality and engineering scores as well as telemetry data of the AUV was transmitted by satellite communication, shown in the enlargement at the bottom left in Fig. 9. The telemetry data showed good altitude keeping with the minimum recorded altitudes within expected bounds, giving confidence in the performance of the AUV. The image scores showed that the lasers and strobes were working fine, but that the image quality was below ideal levels. If possible, the mapping altitude would be lowered in such a case. However, because of the presence of artificial objects protruding vertically from the seafloor in the area, the same mapping altitude was kept for the remaining dives at that site (M79–M82) for safety reasons.

After successfully completing all three planned grid mapping dives, ALR returned to Shetland after 8 days and 18 hours of continuous operation and 453 km of distance

traveled. It was recovered, recharged and the full AUV navigation and BioCam imagery data was downloaded. Fig. 10(a) shows the image quality scores transmitted via satellite communication while at the site, which are consistent with the scores from the full dataset downloaded after recovery of the AUV. It also shows that for a given mapping altitude the quality scores are in general lower than for the medium turbidity reference data and significantly lower than those for the low turbidity reference data. Water turbidity at a given location changes due to influences such as weather and tidal currents, which explains why the average quality scores change between dives despite the dive sites and the data acquisition altitudes being the same. The full AUV navigation data were also downloaded, which showed good altitude keeping throughout all dives, confirming what the heavily downsampled data transmitted via satellite had already indicated.

**TABLE 2.** Statistics of ALR-BioCam dives. NWH: North West Hutton, MIL: Miller, BPM: Braemar Pockmarks MPA.

| Dive | Location | Duration | No. strobed images | No. laser line images | Mapping alt. (m) | Mapped area (m$^2$) |
|------|----------|----------|--------------------|-----------------------|------------------|---------------------|
| M78 | NWH | 12h 16min 48s | 13198 | 386681 | 5 | 190672 |
| M79 | NWH | 1h 47min 24s | 947 | 27758 | 5 | 11344 |
| M80 | NWH | 12h 37min 48s | 13655 | 400014 | 5 | 186404 |
| M81 | NWH | 1h 39min 36s | 660 | 19363 | 5 | 8165 |
| M82 | NWH | 7h 22min 12s | 7325 | 214711 | 5 | 98277 |
| M93 | MIL | 8h 10s | 8684 | 254534 | 5 | 118270 |
| M94 | MIL | 7h 44min 37s | 8456 | 247771 | 4.6 | 111348 |
| M95 | MIL | 7h 46min 48s | 7776 | 228112 | 4 | 93796 |
| M97 | BPM | 6h 52s | 6049 | 177263 | 5 | 73062 |
| **Total** | - | **65h 16min 15s** | **66750** | **1956207** | - | **891338** |
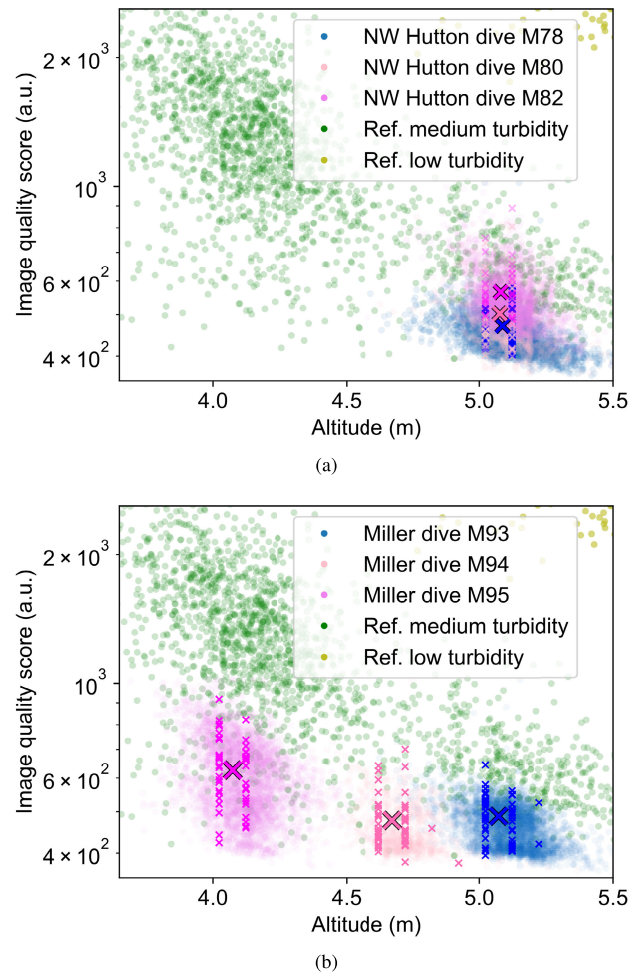


**FIGURE 10.** Laser image scores for two sites mapped during the INSITE AT-SEA deployment. The crosses are the values transmitted via satellite communication, with the larger crosses indicating their average. The dots are the full data downloaded postrecovery of the AUV. (a) Scores from three dives at the NW Hutton site. (b) Scores from three dives at the Miller site.
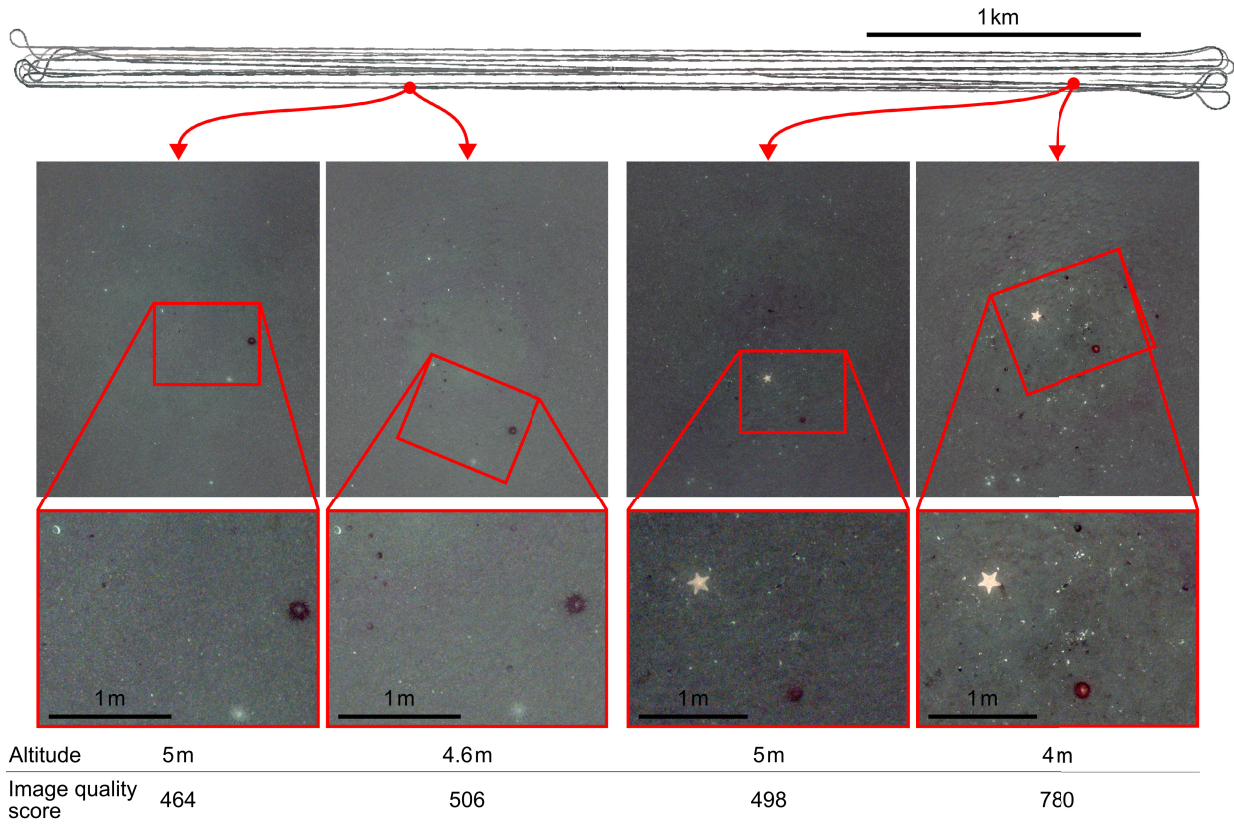
ALR-BioCam were then deployed on the second leg where they first mapped another former oil exploration site at the Miller oilfield, before mapping several transects in a single dive in the Braemar Pockmarks MPA. At the time of deployment a large storm with predicted 100 km/h wind speeds and 7 m wave height was approaching Shetland. The AUV was deployed before the weather window shut while the sea was still calm and programmed to head toward the survey site, but to stay at depth while the storm passed. The dark blue shaded area in Fig. 9 highlights the time window of the storm, with the depth-below-sea surface measurements varying slightly during this period, due to the large waves at the surface. The summary of image scores received via satellite communication after the first dive (M93) from an altitude of 5 m at Miller shown as blue crosses in Fig. 10(b) again reported lower than ideal image quality scores. As the navigation data confirmed reliable altitude keeping, with the lowest recorded distance over ground consistently larger than 4.4 m as the purple markers for dive M93 in Fig. 9, the mapping altitude was set to 4.6 m for the second dive (M94) and to 4 m for the third dive (M95) at the site. While the first reduction in altitude did not lead to a noticeable difference in reported image quality, which could be due to small changes in the water turbidity, the second, bigger reduction in altitude led to a clear improvement as the pink markers in Fig. 10(b).

ALR was then piloted to a third site, Braemar Pockmarks, where it conducted another dive (M97), mapping at a 5 m requested altitude. The AUV ended the dive early, and the satellite transmitted data showed the AUV had flown below the minimum acceptable altitude for longer than the 10 s persistence triggering an early surface, which, as became clear after downloading the data postrecovery, was due to the sudden change in topography at a deep pockmark. The satellite-transmitted compressed navigation data showed good altitude keeping and performance up until the sudden altitude underrun. The limited data at the spatial and temporal resolution that could be transmitted by satellite communication did not provide sufficient detail to remotely identify the cause of the unexpected behavior and no further dives were conducted at the site, as per the protocol outlined in Section IV-E. ALR was piloted back to Shetland where it was recovered after having covered 560 km in 12 days and 19 h

**TABLE 3.** Comparison of transmitted image scores to those logged on the device.

| Dive | Quality scores | | | | | Engineering scores | | | | |
|------|------------------|------------------|----------------|----------------|------|--------------------|------------------|----------------|----------------|------|
| | $\mu_{transm.}$ | $\sigma_{transm.}$ | $\mu_{logged}$ | $\sigma_{logged}$ | $t$ | $\mu_{transm.}$ | $\sigma_{transm.}$ | $\mu_{logged}$ | $\sigma_{logged}$ | $t$ |
| M78 | 469.0 | 46.4 | 467.8 | 38.2 | -0.2 | 5237.2 | 571.1 | 5315.2 | 188.0 | 1.0 |
| M80 | 500.4 | 89.2 | 500.7 | 86.8 | 0.0 | 5173.1 | 606.6 | 5232.6 | 219.4 | 0.7 |
| M82 | 558.2 | 80.3 | 568.3 | 71.0 | 0.8 | 5048.9 | 606.4 | 5129.7 | 150.9 | 0.9 |
| M93 | 485.7 | 60.5 | 484.5 | 58.9 | -0.1 | 4452.6 | 510.4 | 4512.4 | 172.7 | 0.8 |
| M94 | 474.2 | 67.7 | 479.7 | 67.2 | 0.6 | 5145.4 | 627.9 | 5232.1 | 241.2 | 1.0 |
| M95 | 626.8 | 112.1 | 629.1 | 125.0 | 0.1 | 6489.9 | 873.3 | 6642.0 | 369.0 | 1.2 |
| M97 | N/A | N/A | 433.5 | 38.4 | N/A | N/A | N/A | 4893.0 | 274.8 | N/A |



| Altitude | 5 m | 4.6 m | 5 m | 4 m |
|----------|-----|-------|-----|-----|
| Image quality score | 464 | 506 | 498 | 780 |

**FIGURE 11.** Top view of the reconstruction of the Miller dive site with strobed color photographs from different altitudes (5 m: dive M93, 4.6 m: dive M94, and 4 m: dive M95) showing the same areas. There is a clear reduction in image noise and improvement of image detail in the photographs taken from the lower altitudes, which is reflected in the image score.

and conducted four dives, on top of the five dives from the first leg, as listed in Table 2, bringing the total mapped area to over 89 hectares.

Table 3 shows the means ($\mu$) and standard deviations ($\sigma$) of the quality and engineering scores when the AUV was at depth during the main mapping dives (not including M79 and M81, which were transits between grid-survey areas). The Student's t-test values ($t$) show that the distributions of the transmitted score samples align with the distributions of the much larger number of scores logged on the device. Although the standard deviation of the transmitted score samples is in general higher than for the logged scores, this is expected, as the standard deviation decreases with the increasing number of samples. While a narrow distribution of image scores implies uniform conditions, a high variance is indicative of diverse seafloor cover or multiple substrate types that are well visible in the camera images. For example, scattered shells on a silty seafloor as observed at the Miller site (see Fig. 11) can lead to this. This effect is more pronounced for the quality score, as only a small area of the seafloor is illuminated by the sheet laser, and the presence or absence of bright objects in this area has a significant influence on the score for a particular image. It is also more pronounced in clearer imaging conditions, as turbidity has the effect of lowering the image contrast. Provided that the transmitted scores show no obvious signs of outliers, its average score is therefore a reasonable indicator even when the variance is relatively high.
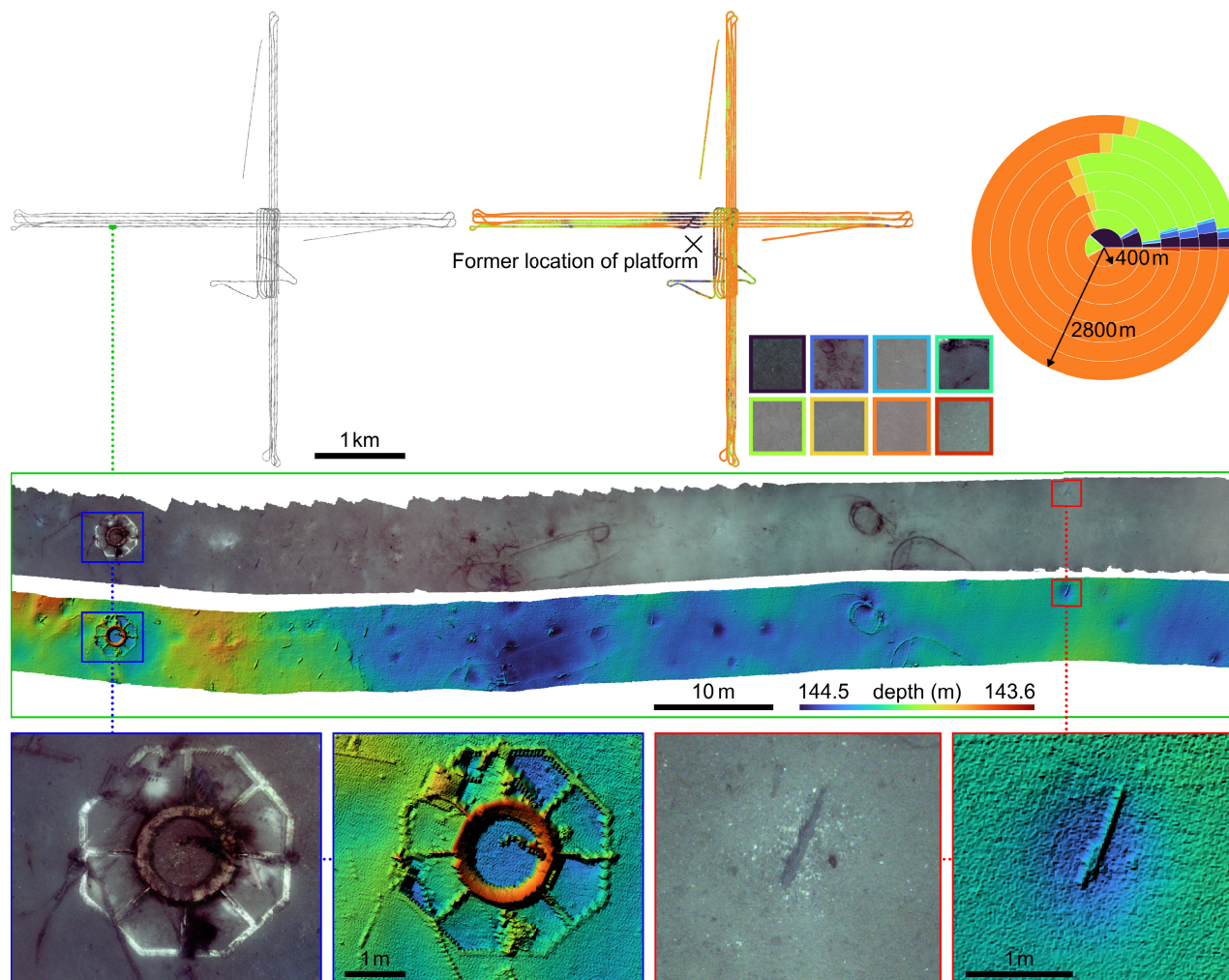
**FIGURE 12.** Three-dimensional reconstruction of the seafloor at the North West Hutton site mapped during dives M78 to M82 with texture and microbathymetry maps at different zoom levels. The image in the center at the top shows the georeferenced classification of the seafloor photographs and the pie chart to its right the portion of each class within the mapped area for different distances from the former location of the platform.

Fig. 11 shows a top view of the reconstruction of the Miller site generated based on the data from the three dives at the site, generated from the full data downloaded after recovering the AUV. Photographs taken of the same location from different mapping altitudes show the change in image quality reflected in the level of detail visible and the amount of marine snow in the final processed images, highlighting the importance of ensuring the raw collected data is of sufficient quality.

While the strobed color photographs from the NW Hutton dive site suffered from higher levels of noise than at the Miller site, its strong visual features, including artificial structures, pipes, and large organisms found at the site are clearly discernible also in the less optimal conditions as shown in Fig. 12. In addition, the 3-D relief of the seafloor and the objects on it was more pronounced and was mapped by the laser line-based 3-D reconstruction algorithm in high detail, virtually undisturbed by the higher level of turbidity, as the laser line images are less affected by it. The 3-D

reconstruction shows a guide base from the decommissioned oil and gas infrastructure, as well as several tens of meters of pipes, but also scores of ~1-m length common ling (*Molva molva*) nesting in the area. While it is not obvious from the photographs alone, the 3-D reconstruction shows that the fish live in burrows with diameters up to 1.5 m and depths of up to 20 cm. Other features observed at the site were boulders from rock dumps, discolored sediments, and seafloor cables, among others.

As an example of automated information extraction from mapping data, the algorithm described in Section III-C was used to automatically classify the seafloor photographs. The georeferenced results are shown at the top-center of Fig. 12 with representative images for each class shown below. This enables further data analysis and statistics of the mapped area. The pie chart in the top-right of the figure shows an example where the relative distribution of identified classes at different distances from a point (in this case the former location of the oil platform) are identified. Data is split into

**TABLE 4.** Comparison of data volume and theoretical transmission time and associated energy consumption per image for different formats. The JPG and JPEG XL data sizes were determined for a quality setting of 40, and the BPG data size for a quality setting of 30 applied on the set of images from the DY152 cruise. The transmission times assume Iridium SBD messaging with one 1960 B SBD message being sent every 20 s (an optimistic estimate in ideal conditions). The associated energy consumptions assume a power consumption of 10 W for the satellite modem and do not account for the power consumption of any other sensors or actuators.

| Data format | Data size | Transmission time | Energy (J) |
|---|---|---|---|
| Raw (16 bit per pixel) | 10.5 MB | 1 day 7 h 23 min 49 s | 1130286 |
| PNG (lossless compression) | 9.2 MB | 1 day 3 h 15 min 26 s | 981265 |
| JPG (lossy compression) | 328.2 KB | 57 min 10 s | 34297 |
| BPG (lossy compression) | 283.7 KB | 49 min 24 s | 29640 |
| JPEG XL (lossy compression) | 181.6 KB | 31 min 37 s | 18975 |
| Image scores | 4 B | 0.041 s | 0.408 |

bands of distance, each of which covers a range of 400 m and is represented by one ring of the chart. The orange and light green classes, which both represent sediments, are dominant in the entire mapped area, but closer to the former location of the platform the algorithm identified a significantly higher ratio of images belonging to the black class representing discolored sediments, as well as images belonging to the blue and turquoise classes, representing boulders and man-made objects such as pipes, respectively. It has previously been shown that the ability of CNN-based image classifiers to correctly label data degrades with increasing image noise [56], [57], [58]. This highlights the importance of quality-controlling the imagery during data collection to generate this kind of results.

During the 21-day-long campaign covering 1013 km in total, the AUV consumed 21.3 kWh of battery power, corresponding to approximately the energy contained by 2 L of diesel. An equivalent survey deploying an AUV from a research vessel (2000–4000-ton class) would complete the survey faster, approximately five days including transit between sites provided the weather conditions are favorable, but at the same time would use in the order of 10 000 L of fuel per day [59] to power the ship. The shore-launched deployment reduced the fuel consumption and $CO_2$ emissions by approximately three orders of magnitude, and while this reduced the ability for real-time data assessment, the satellite transmitted stats were sufficient to make the correct mission-critical decisions.

## VI. CONCLUSION AND DISCUSSION

Data from the 21-day-long seafloor mapping campaign demonstrates how the image quality score defined in Section II and forwarded to AUV pilots via the workflow explained in Section IV provides a robust way to make informed over-horizon operational decisions for following dives to acquire raw data in the quality suitable for extracting usable and useful information in postprocessing. The proposed measure adds minimal computation overhead and a small amount of payload data that needs to be transmitted via satellite communication, but provides sufficient information to adjust mission parameters and at the same time provides information about the correct functioning of lighting and

cameras. As the algorithm directly works on the raw images, it does not conflate the image quality with the performance of the image reconstruction algorithm or its parameters. Compared to transmitting compressed or uncompressed images, the image scores reduce both the time an AUV needs to spend at the surface for transmitting data, as well as the energy consumed for that, as shown in Table 4. AUV mission planners and pilots take many factors including vehicle dynamics and sensor properties into consideration for balancing the quality and amount of collected data with potential risks to the mission. The in-field vehicle performance details and payload data quality information provided by the proposed method delineate how well this balance is kept. It assists remote piloting of AUVs by providing the necessary feedback for making informed decisions, which with traditional approaches to AUV surveys used to be available only after recovery of the vehicle. It enables multiweek offshore campaigns without a support vessel to collect similar quality data as previously done on surveys with a research ship to support AUV operations.

Collecting data in the North Sea at sites up to 170 km from the launch site without a support vessel led to significant savings of fuel and emitted greenhouse gases, as well as reducing operational logistics and cost. In addition, the AUV could be deployed despite a large storm approaching and make progress on its way to the survey site without being affected—by staying at depth during the time window when the storm passed, something that would not be possible with a small surface vessel. To the best of our knowledge, this was the first time that a former offshore drill site had been visually mapped without a support vessel. The collected imagery gave valuable insights on the distribution of seafloor organisms, infrastructure, and seafloor sediments in the mapped areas. Acting upon the transmitted scores led to a clear improvement of the raw data, reflected in the clarity of the processed images from the Miller site, where the transmitted data after the first dive showed good vehicle performance, but flagged low image quality. The decisions taken by the AUV operators based on this led to the collection of better raw data and ultimately to higher quality output from the survey. While the method has been demonstrated with sheet lasers, it could potentially also be applied in a similar fashion on camera systems with laser

pointers, such as scaling lasers. However, the narrower beam would make it more susceptible to occlusions, and further studies would have to be conducted to determine potential applications.

Pressure to save costs and to progress toward the net zero goals motivate the development of noninvasive, economical, and environmentally sustainable survey practices. While these are not likely to fully replace traditional survey methods, increasing the range of ship-free data acquisition methods that can gather useful information can reduce the duration or frequency of traditional surveys. While satellite communication has seen the coverage and communication speed increase, the significantly higher data acquisition rate (8.3 MB/s for the system used in this research) compared to satellite transmission rate (1.1 kB/s for the system used in this research) for compact, deep dive compatible antennae means that full, uncompressed data cannot be transmitted in the foreseeable future and methods for compressing data will continue to play an important role. The proposed method also has potential real-time applications where the AUV could change the altitude or lighting and camera settings as a function of the returned score, without the human in the loop.

## ACKNOWLEDGMENT

## REFERENCES

[1] N. Agarwala, "Monitoring the ocean environment using robotic systems: Advancements, trends, and challenges," *Mar. Technol. Soc. J.*, vol. 54, no. 5, pp. 42–60, Sep. 2020. [Online]. Available: https://www.ingentaconnect.com/content/10.4031/MTSJ.54.5.7

[2] P. J. Bernalte Sánchez, M. Papaelias, and F. P. G. Márquez, "Autonomous underwater vehicles: Instrumentation and measurements," *IEEE Instrum. Meas. Mag.*, vol. 23, no. 2, pp. 105–114, Apr. 2020. [Online]. Available: https://ieeexplore.ieee.org/document/9062680/

[3] O. Khalid et al., "Applications of robotics in floating offshore wind farm operations and maintenance: Literature review and trends," *Wind Energy*, vol. 25, no. 11, pp. 1880–1899, Nov. 2022, doi: 10.1002/we.2773.

[4] R. Eustice, H. Singh, J. Leonard, M. Walter, and R. Ballard, "Visually navigating the RMS Titanic with SLAM information filters," in *Robotics: Science and Systems I*. Cambridge, MA, USA: MIT Press, Jun. 2005. [Online]. Available: http://www.roboticsproceedings.org/rss01/p08.pdf

[5] M. Woolsey and A. Woolsey, "Using MB-system and MATLAB to generate geographical mosaics from seafloor images," in *Proc. OCEANS MTS/IEEE Monterey*, Sep. 2016, pp. 1–10. [Online]. Available: http://ieeexplore.ieee.org/document/7761283/

[6] H. Singh, C. Roman, O. Pizarro, R. Eustice, and A. Can, "Towards high-resolution imaging from underwater vehicles," *Int. J. Robot. Res.*, vol. 26, no. 1, pp. 55–74, Jan. 2007, doi: 10.1177/0278364907074473.

[7] M. Johnson-Roberson, O. Pizarro, S. B. Williams, and I. Mahon, "Generation and visualization of large-scale three-dimensional reconstructions from underwater robotic surveys," *J. Field Robot.*, vol. 27, no. 1,

pp. 21–51, Jan. 2010, doi: 10.1002/rob.20324.

[8] A. Bodenmann, B. Thornton, and T. Ura, "Generation of high-resolution three-dimensional reconstructions of the seafloor in color using a single camera and structured light," *J. Field Robot.*, vol. 34, no. 5, pp. 833–851, 2017.

[9] T. Yamada et al., "GeoCLR: Georeference contrastive learning for efficient seafloor image interpretation," *Field Robot.*, vol. 2, pp. 1134–1155, Mar. 2022. [Online]. Available: https://fieldrobotics.net/Field_Robotics/Volume_2_files/Vol2_37.pdf

[10] B. Mbani, T. Schoening, I.-Z. Gazis, R. Koch, and J. Greinert, "Implementation of an automated workflow for image-based seafloor classification with examples from manganese-nodule covered seabed areas in the central Pacific ocean," *Sci. Rep.*, vol. 12, no. 1, p. 15338, Sep. 2022. [Online]. Available: https://www.nature.com/articles/s41598-022-19070-2

[11] S. B. Williams et al., "Monitoring of benthic reference sites: Using an autonomous underwater vehicle," *IEEE Robot. Autom. Mag.*, vol. 19, no. 1, pp. 73–84, Mar. 2012. [Online]. Available: https://ieeexplore.ieee.org/document/6174326/

[12] A. Bodenmann et al., "High-resolution visual seafloor mapping and classification using long range capable AUV for ship-free benthic surveys," in *Proc. IEEE Underwater Technol. (UT)*, Mar. 2023, pp. 1–6. [Online]. Available: https://ieeexplore.ieee.org/document/10103421/

[13] Y. Zarayskaya et al., "GEBCO-NF alumni team technology solution for shell ocean discovery XPRIZE final round," in *Proc. OCEANS*, Marseille, France, Jun. 2019, pp. 1–10. [Online]. Available: https://ieeexplore.ieee.org/document/8867201/

[14] T. Ohki, H. Kakami, Y. Nishida, T. Nakatani, and B. Thornton, "Development and testing of an unmanned surface towing system for autonomous transport of multiple heterogeneous underwater vehicles for seafloor survey," *Mar. Technol. Soc. J.*, vol. 54, no. 5, pp. 61–71, Sep. 2020.

[15] J. Amos, R. Morelle, and A. Francis, "Robot ships: Huge remote controlled vessels are setting sail," *BBC Sci. News*, Mar. 2024. [Online]. Available: https://www.bbc.co.uk/news/science-environment-68486462

[16] B. W. Hobson, J. G. Bellingham, B. Kieft, R. McEwen, M. Godin, and Y. Zhang, "Tethys-class long range AUVs—Extending the endurance of propeller-driven cruising AUVs from days to weeks," in *Proc. IEEE/OES Auto. Underwater Vehicles (AUV)*, Southampton, U.K., Sep. 2012, pp. 1–8. [Online]. Available: http://ieeexplore.ieee.org/document/6380735/

[17] R. Mills, J. Sobin, R. Patterson, S. Brodet, S. Pilkington, and A. Olsen, "Addressing the need to grow AUV operator workforce: Advanced autonomy and goal based mission planning," in *Proc. OCEANS-MTS/IEEE U.S. Gulf Coast*, Biloxi, MS, USA, Sep. 2023, pp. 1–6. [Online]. Available: https://ieeexplore.ieee.org/document/10337110/

[18] D. Roper et al., "Autosub long range 6000: A multiple-month endurance AUV for deep-ocean monitoring and survey," *IEEE J. Ocean. Eng.*, vol. 46, no. 4, pp. 1179–1191, Oct. 2021.

[19] A. B. Phillips et al., "Autosub long range 1500: A continuous 2000 km field trial," *Ocean Eng.*, vol. 280, Jul. 2023, Art. no. 114626. [Online]. Available: https://www.sciencedirect.com/science/article/pii/S0029801823010107

[20] D. R. Yoerger, A. M. Bradley, B. B. Walden, H. Singh, and R. Bachmayer, "Surveying a subsea lava flow using the autonomous benthic explorer (ABE)," *Int. J. Syst. Sci.*, vol. 29, no. 10, pp. 1031–1044, Oct. 1998, doi: 10.1080/00207729808929596.

[21] H. Kondo, T. Ura, and Y. Nose, "Development of autonomous underwater vehicle," *J. Robot. Mechatronics*, vol. 13, no. 2, pp. 205–211, Apr. 2001. [Online]. Available: https://www.fujipress.jp/jrm/rb/robot001300020205

[22] D. R. Yoerger, A. M. Bradley, S. C. Martin, and L. L. Whitcomb, "The sentry autonomous underwater vehicle: Field trial results and future capabilities," in *Proc. AGUFM*, 2006, p. 1674. [Online]. Available: https://ui.adsabs.harvard.edu/abs/2006AGUFMOS33A1674Y/abstract

[23] T. Nakatani et al., "AUV," TUNA-SAND and its exploration of hydrothermal vents at Kagoshima Bay," in *Proc. MTS/IEEE Oceans*, Kobe, Japan, 2008, pp. 1–5. [Online]. Available: https://ieeexplore.ieee.org/xpl/articleDetails.jsp

[24] S. B. Williams et al., "Autonomous underwater vehicle–assisted surveying of drowned reefs on the shelf edge of the great barrier reef, Australia," *J. Field Robot.*, vol. 27, no. 5, pp. 675–697, Sep. 2010, doi: 10.1002/rob.20356.

[25] P. L. N. Carrasco, F. Bonin-Font, M. M. Campos, and G. O. Codina, "Stereo-vision graph-SLAM for robust navigation of the AUV SPARUS II," in *Proc. 4th IFAC Workshop Navigat., Guid. Control Underwater Vehicles*, vol. 48. Amsterdam, The Netherlands: Elsevier, Apr. 2015, pp. 200–205. [Online]. Available: https://www.sciencedirect.com/science/article/pii/S2405896315002724

[26] U. Neettiyath, H. Sugimatsu, T. Koike, K. Nagano, T. Ura, and B. Thornton, "Multirobot multimodal deep sea surveys: Use in detailed estimation of manganese crust distribution," *IEEE Robot. Autom. Mag.*, vol. 31, no. 1, pp. 84–95, Mar. 2024.

[27] D. Berman, D. Levy, S. Avidan, and T. Treibitz, "Underwater single image color restoration using haze-lines and a new quantitative dataset," *IEEE Trans. Pattern Anal. Mach. Intell.*, vol. 43, no. 8, pp. 2822–2837, Aug. 2020. [Online]. Available: https://ieeexplore.ieee.org/document/9020130/

[28] M. Bryson, M. Johnson-Roberson, O. Pizarro, and S. B. Williams, "True color correction of autonomous underwater vehicle imagery," *J. Field Robot.*, vol. 33, no. 6, pp. 853–874, Sep. 2016, doi: 10.1002/rob.21638.

[29] D. Akkaynak and T. Treibitz, "Sea-thru: A method for removing water from underwater images," in *Proc. IEEE/CVF Conf. Comput. Vis. Pattern Recognit. (CVPR)*, Long Beach, CA, USA, Jun. 2019, pp. 1682–1691.

[30] G. West, A. Bodenmann, D. Newborough, and B. Thornton, "Resolution and coverage—The best of both worlds in the BioCam 3D visual mapping project," *J. Ocean Technol.*, vol. 15, no. 3, pp. 67–76, 2020. [Online]. Available: https://www.thejot.net/article-preview/?show_article_preview=1186&jot_download_article=1186

[31] D. F. Hoag, V. K. Ingle, and R. J. Gaudette, "Low-bit-rate coding of underwater video using wavelet-based compression algorithms," *IEEE J. Ocean. Eng.*, vol. 22, no. 2, pp. 393–400, Apr. 1997. [Online]. Available: http://ieeexplore.ieee.org/document/585958/

[32] R. L. Eastwood, L. E. Freitag, and J. A. Catipovic, "Compression techniques for improving underwater acoustic transmission of images and data," in *Proc. OCEANS 96 MTS/IEEE Conf. Coastal Ocean-Prospects 21st Century*, Fort Lauderdale, FL, USA, Jul. 1996, pp. 63–67. [Online]. Available: http://ieeexplore.ieee.org/document/566719/

[33] J. W. Kaeli, J. J. Leonard, and H. Singh, "Visual summaries for low-bandwidth semantic mapping with autonomous underwater vehicles," in *Proc. IEEE/OES Auto. Underwater Vehicles (AUV)*, Oct. 2014, pp. 1–7. [Online]. Available: http://ieeexplore.ieee.org/document/7054429/

[34] C. Murphy, J. M. Walls, T. Schneider, R. M. Eustice, M. Stojanovic, and H. Singh, "CAPTURE: A communications architecture for progressive transmission via underwater relays with eavesdropping," *IEEE J. Ocean. Eng.*, vol. 39, no. 1, pp. 120–130, Jan. 2014. [Online]. Available: http://ieeexplore.ieee.org/document/6570549/

[35] J. Ahn, S. Yasukawa, T. Sonoda, Y. Nishida, K. Ishii, and T. Ura, "An optical image transmission system for deep sea creature sampling missions using autonomous underwater vehicle," *IEEE J. Ocean. Eng.*, vol. 45, no. 2, pp. 350–361, Apr. 2020. [Online]. Available: https://ieeexplore.ieee.org/document/8516295/

[36] Z. Wang and A. C. Bovik, *Modern Image Quality Assessment* (Synthesis Lectures on Image, Video, and Multimedia Processing). Cham, Switzerland: Springer, 2006. [Online]. Available: https://link.springer.com/10.1007/978-3-031-02238-8

[37] A. K. Moorthy and A. C. Bovik, "A two-step framework for constructing blind image quality indices," *IEEE Signal Process. Lett.*, vol. 17, no. 5, pp. 513–516, May 2010. [Online]. Available: http://ieeexplore.ieee.org/document/5432998/

[38] A. K. Moorthy and A. C. Bovik, "Blind image quality assessment: From natural scene statistics to perceptual quality," *IEEE Trans. Image Process.*, vol. 20, no. 12, pp. 3350–3364, Dec. 2011. [Online]. Available: http://ieeexplore.ieee.org/document/5756237/

[39] H. Tang, N. Joshi, and A. Kapoor, "Learning a blind measure of perceptual image quality," in *Proc. CVPR*, Colorado Springs, CO, USA, Jun. 2011, pp. 305–312. [Online]. Available: http://ieeexplore.ieee.org/document/5995446/

[40] A. Mittal, A. K. Moorthy, and A. C. Bovik, "No-reference image quality assessment in the spatial domain," *IEEE Trans. Image Process.*, vol. 21, no. 12, pp. 4695–4708, Dec. 2012. [Online]. Available: http://ieeexplore.ieee.org/document/6272356/

[41] A. Mittal, R. Soundararajan, and A. C. Bovik, "Making a 'completely blind' image quality analyzer," *IEEE Signal Process. Lett.*, vol. 20, no. 3, pp. 209–212, Mar. 2013. [Online]. Available: http://ieeexplore.ieee.org/document/6353522/

[42] N. Venkatanath, D. Venkatanath, M. Chandrasekhar, S. S. Channappayya, and S. S. Medasani, "Blind image quality evaluation using perception based features," in *Proc. 21st Nat. Conf. Commun. (NCC)*, Feb. 2015, pp. 1–6. [Online]. Available: http://ieeexplore.ieee.org/document/7084843/

[43] M. Yang and A. Sowmya, "An underwater color image quality evaluation metric," *IEEE Trans. Image Process.*, vol. 24, no. 12, pp. 6062–6071, Dec. 2015. [Online]. Available: http://ieeexplore.ieee.org/document/7300447/

[44] K. Panetta, C. Gao, and S. Agaian, "Human-visual-system-inspired underwater image quality measures," *IEEE J. Ocean. Eng.*, vol. 41, no. 3, pp. 541–551, Jul. 2016. [Online]. Available: http://ieeexplore.ieee.org/document/7305804/

[45] N. Yang, Q. Zhong, K. Li, R. Cong, Y. Zhao, and S. Kwong, "A reference-free underwater image quality assessment metric in frequency domain," *Signal Process., Image Commun.*, vol. 94, May 2021, Art. no. 116218. [Online]. Available: https://www.sciencedirect.com/science/article/pii/S0923596521000503

[46] Y. Wang et al., "An imaging-inspired no-reference underwater color image quality assessment metric," *Comput. Electr. Eng.*, vol. 70, pp. 904–913, Aug. 2018. [Online]. Available: https://www.sciencedirect.com/science/article/pii/S0045790617324953

[47] T. Chen, X. Yang, N. Li, T. Wang, and G. Ji, "Underwater image quality assessment method based on color space multi-feature fusion," *Sci. Rep.*, vol. 13, no. 1, p. 16838, Oct. 2023. [Online]. Available: https://www.nature.com/articles/s41598-023-44179-3

[48] G. Hou, S. Zhang, T. Lu, Y. Li, Z. Pan, and B. Huang, "No-reference quality assessment for underwater images," *Comput. Electr. Eng.*, vol. 118, Aug. 2024, Art. no. 109293. [Online]. Available: https://www.sciencedirect.com/science/article/pii/S0045790624002210

[49] X. Chu, R. Hu, Y. Liu, J. Cao, and L. Xu, "SISC: A feature interaction-based metric for underwater image quality assessment," *IEEE J. Ocean. Eng.*, vol. 49, no. 2, pp. 637–648, Apr. 2024. [Online]. Available: https://ieeexplore.ieee.org/document/10376401/

[50] Z. Wang, L. Shen, Z. Wang, Y. Lin, and J. Chen, "Prior-based underwater enhanced image quality assessment network," *IEEE J. Ocean. Eng.*, vol. 49, no. 2, pp. 592–605, Apr. 2024. [Online]. Available: https://ieeexplore.ieee.org/document/10436665/

[51] J. S. Jaffe, "Computer modeling and the design of optimal underwater imaging systems," *IEEE J. Ocean. Eng.*, vol. 15, no. 2, pp. 101–111, Apr. 1990. [Online]. Available: http://ieeexplore.ieee.org/xpls/abs_all.jsp?arnumber=50695

[52] M. Massot-Campos, T. Yamada, and B. Thornton, "Towards sensor agnostic artificial intelligence for underwater imagery," in *Proc. IEEE Underwater Technol. (UT)*, Mar. 2023, pp. 1–6. [Online]. Available: https://ieeexplore.ieee.org/document/10103403/

[53] T. Yamada, M. Massot-Campos, A. Prügel-Bennett, O. Pizarro, S. B. Williams, and B. Thornton, "Guiding labelling effort for efficient learning with georeferenced images," *IEEE Trans. Pattern Anal. Mach. Intell.*, vol. 45, no. 1, pp. 593–607, Jan. 2023. [Online]. Available: https://ieeexplore.ieee.org/document/9669070/

[54] A. Munafo et al., "The NOCS on-board control system," in *Proc. OCEANS-Marseille*, Jun. 2019, pp. 1–8. [Online]. Available: https://ieeexplore.ieee.org/document/8867412/

[55] C. A. Harris et al., "Oceanids C2: An integrated command, control, and data infrastructure for the over-the-horizon operation of marine autonomous systems," *Frontiers Mar. Sci.*, vol. 7, p. 397, Jun. 2020. [Online]. Available: https://www.frontiersin.org/articles/10.3389/fmars.2020.00397

[56] S. Dodge and L. Karam, "Understanding how image quality affects deep neural networks," in *Proc. 8th Int. Conf. Quality Multimedia Exp. (QoMEX)*, Lisbon, Portugal, Jul. 2016, pp. 1–6. [Online]. Available: http://ieeexplore.ieee.org/document/7498955/

[57] Y. Pei, Y. Huang, Q. Zou, X. Zhang, and S. Wang, "Effects of image degradation and degradation removal to CNN-based image classification," *IEEE Trans. Pattern Anal. Mach. Intell.*, vol. 43, no. 4, pp. 1239–1253, Apr. 2021. [Online]. Available: https://ieeexplore.ieee.org/document/8889765/

[58] J. De Hoog, A. Anwar, P. Reiter, S. Mercelis, and P. Hellinckx, "Metamodelling of noise to image classification performance," *IEEE Access*, vol. 11, pp. 47994–48006, 2023. [Online]. Available: https://ieeexplore.ieee.org/document/10117595/

[59] Schmidt Ocean Inst. (2024). *Ship Specifications—Schmidt Ocean Institute*. Accessed: Jul. 4, 2024. [Online]. Available: https://schmidtocean.org/rv-falkor/ship-specifications/

• • •